Elucidating the impact of Li_3InCl_6-coated $LiNi_{0.8}Co_{0.15}Al_{0.05}O_2$ on the electro-chemo mechanics of Li_6PS_5Cl-based solid-state batteries

Feng Jin[1], Laras Fadillah[1], Hung Quoc Nguyen[1], Torgeir Matre Sandvik[1], Yu Liu[1], Adrian Gacia-Martin[2,3], Elena Salagre[2,3], Enrique G. Michel[2,3], Dragos Stoian[4], Kenneth Marshall[4], Wouter Van Beek[4], Guenther Redhammer[5], Mir Mehraj Ud Din[1,6], and Daniel Rettenwander[1,6] *

[1]Department of Material Science and Engineering, NTNU Norwegian University of Science and Technology, Trondheim, Norway
[2]Departamento de Fisica de la Materia Condensada, Facultad de Ciencias, Universidad Autónoma de Madrid, Madrid, Spain
[3]Condensed Matter Physics Center (IFIMAC), Universidad Autónoma de Madrid, Madrid, Spain
[4]Swiss-Norwegian Beam Lines at European Synchrotron Radiation Facility, 71 Avenue des Martyrs, 38000 Grenoble, France
[5] Department of Chemistry and Physics of Materials, University of Salzburg, 5020, Salzburg, Austria
[6]Christian Doppler Laboratory for Solid-State Batteries, NTNU Norwegian University of Science and Technology, Trondheim, Norway

*Corresponding Author: daniel.rettenwander@ntnu.no

ABSTRACT

Li_6PS_5Cl has attracted much attention due to its high Li-ion conductivity and ease in processibility, which allows large-scale applications of solid-state batteries. However, when combined with high-voltage cathodes, Li_6PS_5Cl suffers from detrimental side reactions. Due to the stability towards high voltages combined with a relatively high Li-ion conductivity Li_3InCl_6 has been considered as catholyte with the potential to compensate Li_6PS_5Cl shortcomings. Despite previous claims about its (electro)chemical instability, we hypothesize that Li_3InCl_6 remains a promising choice when (i) triple junctions between Li_3InCl_6, Li_6PS_5Cl, and Ni-rich cathodes are avoided and (ii) the cut-off voltage is below 3.6 V (vs Li/In). Therefore, a core-shell-structured cathode, i.e., $LiNi_{0.8}Co_{0.15}Al_{0.05}O_2$ particles with a 100 nm thick pin-hole-free Li_3InCl_6 layer, has been developed using mechanofusion. When employed in a solid-state battery with a cut-off voltage of 3.58V (vs Li/In) a specific capacity enhancement of about 80 mAh/g at any C-rate (0.1 to 1C) was achieved. The stability of Li_3InCl_6 as well as its functionality to prevent Li_6PS_5Cl from decomposition and cathode particles from mechanical degradation has been demonstrated, by synchrotron operando XRD and, e.g., post-mortem analysis using Plasma FIB SEM and XPS. This study shows that Li_3InCl_6 can be used as catholyte when applied appropriately.

KEYWORDS: solid-state batteries, Li_6PS_5Cl, Li_3InCl_6, coating, mechanofusion

1. INTRODUCTION

Solid-state batteries are considered as one of the most promising next generations of energy storage technologies with a potential to revolutionize electric vehicles (EVs), due to their high energy density and intrinsic safety[1]. Here, the solid electrolyte is key since it allows the utilization of Li or Si as anode and the possibility to have bi-polar cell configurations. Hence, several solid electrolytes have been explored, whereby most of them fall into two groups[2]: (*i*) Oxide-based solid electrolytes, such as garnet-type $Li_7La_3Zr_2O_{12}$ and NaSICON-type $Li_{1+x}Al_xTi_{2-x}(PO_4)_3$ and (*ii*) sulfides, such as thio-LISICON-type $Li_{10}GeP_2S_{12}$ (LGPS) and Argyrodite-type Li_6PS_5Cl (LPSCl). Of most solid electrolytes, LPSCl is considered one of the promising candidates, owing to its high ionic conductivity, favorable mechanical performance, and ease in processing[3]. However, there are significant challenges associated with the energy density, rate capability, and capacity retention of solid-state batteries employing LPSCl[4]. These challenges arise from the interfacial contact-loss during electrochemical cycling as a consequence of volumetric changes in electrodes and the electrochemical stability limitations in the preferred operation voltage range causing undesirable side reactions with high-voltage Ni-rich cathodes, giving rise to fast capacity fade, thus impeding their ultimate commercial realization [5].

To mitigate the challenges associated with interfacial degradation caused by detrimental secondary reactions, the application of a protective coating on the surface of cathode particles is regarded as a productive mitigation strategy[6].Considerable amount of research has been performed to explore suitable coating materials, such as oxides, e.g., ZrO_2[7], HfO_2[8], Li_2ZrO_3[9] and, $LiNbO_3$[10], and phosphates, e.g., Li_3PO_4[11], and $LiZr_2(PO_4)_3$[12]. High-voltage cathodes coated with metal oxides and phosphates show improved specific capacity, and capacity retention compared with uncoated counterparts in thiophosphate-based SSBs. However, these coating additives exhibit either limited Li-ion conductivity ($<10^{-4}$ S/cm), or insufficient stability against high-voltage cathode.

Halides, in particular chlorides, such as Li_3InCl_6 (LIC)[13], Li_3YCl_6[14], Li_3TiCl_6[15] and $Li_{3-x}M_{1-x}Zr_xCl_6$ (M = Y, Er)[16], have gained considerable attention by combining both, high Li-ion conductivities (>0.1 mS/cm) and high-voltage stability (>4.2 V vs Li/Li$^+$). Nevertheless, their instability when paired with Li anode[17] and relatively high production costs limit their application as bulk solid electrolytes. This is, when used as catholyte or in particular coating additive, however, less relevant, which makes them a promising alternative. To avoid direct contact to, e.g., Li, et al[18] proposed a dual electrolyte

2

approach, where LPSCl is used as separator and LIC as catholyte. However, the assembled Li-In|LPSCl|NMC cell has been only functional at elevated temperatures (60 °C), due to the large amount and higher thickness of LIC that result in higher cell impedance. To overcome kinetic limitations Ye, et al. used LPSCl and LIC as catholyte in the NMC composite cathode by using a slurry coating method[19]. They observed an improved initial discharge capacity in their Li-In|LPSCl|NMC cell, when LIC is introduced. However, the long-term electrochemical performance appears to be relatively poor (77.4 % capacity retention after 100 cycles) even at a lower C-rate of 0.1C. The poor cycling performance is likely due to the insufficient covering of NMC particles by LIC during slurry processing causing an irreversible capacity loss as a consequence of electrolyte decomposition. Contrary to these reports, recent studies questioned the compatibility of LIC and LPSCl in Ni-rich-based cathode cells in general. For example, Koc et al found that at a cell potential ≥ 3.65 vs Li/In the decomposition of LIC takes place, as well as a quadruple increase in the interfacial resistance between LIC with LPSCl in a bilayer configuration at 80 °C, indicating not only electrochemical but also chemical instability[20]. This chemical incompatibility between LIC with LPSCl has been proposed to translating into the formation of a passivation interlayer, which leads to degraded electrochemical performance of up to 50 % upon cycling[21]. This chemical instability has been throughout studied subsequently by Rosenbach et al[20] using FIB-SEM combined with TOF-SIMS. They confirmed that LIC with LPSCl are chemically unstable but also highlighted that this degradation is predominant when NMC, LPSCl, and LIC forms triple junction, due to the potential catalytic nature of the cathode. However, they considered their interpretation of findings as highly speculative. Hence, the stability of LIC with LPSCl needs to be further elaborated. Despite this controversial discussion, we conclude that LIC can be used as coating material if (i) triple junction between LIC, LPSCl, and Ni-rich cathodes are avoided and (ii) the cut-off voltage is chosen below 3.6 V (vs Li/in).

Herein, we report on a core-shell structured cathode composite (Fig. 1a), where $LiNi_{0.8}Co_{0.15}Al_{0.05}O_2$ (NCA) particles (core) are coated by a 100 nm thick pin-hole free LIC layer (shell), using a scalable mechanofusion process. Due to the LIC coating interfacial decomposition reactions of LPSCl, interfacial delamination, and particle cracking, as observed for uncoated NCA-based SSBs, are suppressed (Fig. 1b and 1c) facilitates a specific capacity enhancement of about 80 mAh/g for any C-rate and improved long-term cell cycling.

3

2. RESULTS and DISCUSSION

2.1. Development of nanoscale LIC coating material by high-energy ball milling

LIC was synthesized based on a convenient two-step procedure, comprising mechanochemical mixing via high-energy ball milling and subsequent annealing step. The corresponding XRD patterns for LIC before and after annealing are shown in Fig. 1d. Both patterns can be indexed with monoclinic rock-salt structure (space group: *C2/m*). No phases other than LIC can be observed. The surface morphology as shown in SEM image in Fig. 1e reveals the formation of elongated particles of LIC. After annealing LIC shows narrow reflections indicating an increased crystallinity, around 82.5 %. To determine the Li-ion conductivity of LIC, EIS measurements in a temperature range between 25 $^{\circ}$C to 65 $^{\circ}$C were performed. The corresponding Nyquist plots are shown in Figure 1f, revealing one electrical relaxation process: an onset of a high-frequency semicircle and a spike toward low frequencies. Due to the low amount of high-frequency data points, the resistive part of the arc has been simply fitted by a resistance element, which can be attributed to the total Li-ion conduction of the pellet. The low-frequency spike is typically related to the electrodes. Adding another R|CPE element improves the fit due to the non-ideality of the blocking electrode but has no physical meaning. The total Li-ion conductivity of LIC at room temperature was calculated to be 1.44 mS/cm, which is similar to the values reported in the literature[13] and one to two orders in magnitude higher than that of other promising solid electrolyte-based traditional coating candidates, such as garnet-type LLZO[22], NASICON-type LAGP[23], etc. In Fig. 1g the temperature dependence of the Li-ion conductivity is shown. It follows Arrhenius behavior according to $\sigma T = \sigma_0 \exp(-E_a/(k_B T))$, where σ_0 represents the pre-exponential factor. The activation energy E_a is 0.31 eV, which is similar to values reported previously[13].

2.2. Applying LIC as a coating on NMC particles via mechanofusion

LIC was coated around NCA particles via mechanofusion technique (LIC@NCA). Potential changes in phases and crystallinity were further studied via XRD. In Fig. 2a the XRD pattern of LIC@NCA in comparison with NCA is shown. After the coating process, the LIC@NCA was found to retain the pristine layered structure with space group $R\text{-}3m$. No reflections from the LIC were apparent, which may originate from the low weight fraction of the LIC (see Fig. S2-S4 and Tab. S1-S4 for details). Compared to the pristine NCA, LIC@NCA showed a subtle decrease in cell volume from 101.03 Å^3 to 100.97 Å^3. Furthermore, the degree of Ni^{2+}/ Li$^+$ cation mixing (based on the c/a) remained similar for

4

both samples indicating that the crystal structure of NCA remains unaltered after coating NCA particles with LIC. To prove the successful surface coating, SEM studies, on both pristine NCA and LIC@NCA, were conducted. Fig. 2b and Fig. S5a depicts the magnified SEM image of pristine NCA particles, where secondary NCA particles can be clearly observed. In contrast, the magnified SEM image (Fig. 2c and Fig. S5b) of LIC@NCA shows an altered surface morphology with LIC nanoparticles covering the NCA particles surface suggesting a successful coating. The high shear forces created inside the mechanofusion container by high rotational speeds not only causes the particle rounding and coating of LIC nanoparticles onto the NCA particles surface but also enables homogenous and densified LIC coating. To evaluate the uniformity and density of the LIC coating, cross-sectional SEM studies have been performed. As shown in Fig. 2d a ca. 180 nm thick, dense, and uniform LIC coating is evident. Further evidence is given by EDS mapping showing a uniform Cl and In distribution around the NCA particles (Fig. 2e). Additionally, LIC@NCA particle size distribution shared the similar trend with pristine NCA (Fig. S6).

The surface chemistry of LIC, pristine NCA and LIC@NCA was studied via XPS as shown in Fig.2. The In 3d spectrum displays a doublet with a single component and peaks located at 453.8 eV (In $3d_{3/2}$) and 446.2 eV (In $3d_{5/2}$) (Fig. 2i). The Cl 2p spectrum also displays a doublet with a single component with peaks at 201.2 eV (Cl $2p_{1/2}$) and 199.5 eV (Cl $2p_{1/2}$) (Fig. 2j). These components can be assigned to the In^{3+} and Cl^- chemical bonding states in LIC, respectively. Ni 2p and Co 2p core levels from the bare NCA cathode were studied as well. According to the spectrum of Ni 2p (Fig. 2k), two components appear at 854.6 eV and 856.6 eV, assigned to Ni^{2+} and Ni^{3+}, respectively[24], an indication of mixed valence[24-25]. The observation of Ni 2p and Co 2p core levels from LIC@NCA is difficult because the surface sensitivity of XPS significantly decreases their intensity. In turn, the observation of these peaks in LIC@NCA (Fig. 2i, j) with a similar line shape (in the case of Ni 2p) and with a strongly damped intensity in both cases, compared with pristine NCA (Fig. 2k, l), indicates that NCA is shielded by LIC, which gives further evidence for the successful coating.

2.3. Electrochemical evaluation and battery testing

To evaluate the functionality of LIC as a protective coating the electrochemical performance in solid-state batteries using NCA (SSB-NCA) and LIC@NCA (SSB-LIC@NCA) has been tested (see details in the experimental section and Fig. S7).

5

The initial charge and discharge curves of SSBs recorded at 0.1C with cut-off voltage of 4.2 V (vs. Li$^+$/Li) are presented in Fig. 3a. It is evident that for SSB-LIC@NCA the polarization during charge and discharge is effectively suppressed and the discharge capacity is significantly increased (from 71.8 mAh/g for SSB-NCA to 148.3 mAh/g for SSB-LIC@NCA). Moreover, SSB-LIC@NCA shows significantly more stable long-term cycling at around 133.6 mAh/g and 80.1% capacity retention at 0.2 C compared to SSB-NCA with around 40 mAh/g for 200 cycles (Fig. 3a-d).

The charge/discharge profiles together with the cycle performance under different C-rates (i.e., 0.1C, 0.2C, 0.5C, and 1C) are shown in Fig. 3b and Fig. 3c, respectively. It is evident that SSB-LIC@NCA exhibit higher capacity at any current density (about 80 mAh/g at any rate). In detail, the initial charge capacity for LIC@NCA compared to NCA is markedly increased from 71.8 mAh/g to 148.3 mAh/g at 0.1 C, from 42.8 mAh/g to 133.6 mAh/g at 0.2 C, from 8.4 mAh/g to 104.2 mAh/g at 0.5C, and from 0.2 mAh/g to 74.3 mAh/g at 1 C. The high polarization could be related to the instability of LPSCl against NCA, which leads to its decomposition and formation of a highly resistive interphase.[26] The formation of such a resistive interlayer is evident from the impedance spectroscopy analysis conducted for both pristine NCA and LIC@NCA before and after cycling. The corresponding impedance spectra of the cells in the bode plot representation are shown in Fig. 3e, f. Both cells exhibit two characteristic plateaus, whereby the high-frequency plateau represents the resistance of the electrolyte and the low-frequency plateau the interfacial impedance between the electrolyte and the electrode material. Here, the bulk resistances for SSB-NCA and SSB-LIC@NCA are similar (~44 Ω), while the interface resistance for SSB-LIC@NCA increased slightly (~20 Ω), which is associated with the LIC coating (Fig. 3g). The total resistance of the cell is about 120 Ω, suggesting that the overpotential of the cell is dominated by the cell resistance. Despite the higher initial cell resistance of SSB-LIC@NCA the interfacial resistance of SSB-NCA is significantly increased already after the first cycle, which can be associated with interfacial degradation processes. This increase is even more pronounced after 100 cycles, where the resistance reaches values around 4813 Ω in contrast to SSB-LIC@NCA with a resistance of about 267 Ω (see Fig. 3g). An incremental increase in the interfacial resistance of SSB-LIC@NCA suggest that LIC coating can hinder or at least slow down interfacial degradation processes, and consequently improves the specific capacity and rate performance.

2.4. Origin of cell performance improvement

To understand the interfacial degradation processes and the mechanism of suppression promoted by LIC coating, the morphological and chemical degradation processes have been studied via SEM and PFIB-SEM, XPS, and operando synchrotron XRD.

Operando synchrotron XRD data recorded during the first cycle show similar behavior in the structural and phase evolution of NCA for SSB-NCA and SSB-LIC@NCA (Fig. 4a-c and Fig. 4e-g; see details about the analysis in Supplementary Note 1, Fig. S13-S16). Interestingly, the charging process is significantly delayed in the initial cycle of SSB-NCA (Fig. 4a-c). At about 3 V a sloping region occurs, similar to what has been reported previously[21]. During the beginning of the charging process, the lattice parameters *a* and *c* remained almost the same while the rapid non-linear change in lattice parameters were observed as the charging process continued. The time dependence of the lattice parameter points to a growing SEI layer, since as the thickness of the SEI increases the polarization follows, hence, the accessible capacity and correspondingly the changes in lattice parameter decreases. Although no phases (Fig. 4i, j) other than NCA and LPSCl have been observed by XRD (potentially related to the detection limit), the degradation of LPSCl and the formation of passivating interphases is evident from XPS and SEM analysis. As shown in Fig. 5a, d, e, cathode particles are compactly embedded in the LPSCl matrix. The situation changes after 200 cycles when NCA secondary particles were fractured and dispersed into the LPSCl matrix with significant contact loss (Fig. 5f-j). Moreover, LPSCl particles alter their shape from roundish to needle structure (Fig. 5a-b and Fig. S1a-c) and significant changes in chemistry takes place (Fig. 4l, m). For LPSCl powder the S 2p spectrum shows two doublets. The main one at 161.4 (S $2p_{3/2}$) is related to PS_4^{3-}. A minor second doublet appears at 160.1 eV (S $2p_{3/2}$)[8]. It corresponds to S^{2-}, which originates from the Li_2S precursor[8]. In the corresponding P 2p spectrum, a single doublet at 131.7 eV (P $2p_{3/2}$) appears, which can be assigned to the PS_4^{3-} compounds[27]. In cycled SSB-NCA a significant amount of new peaks appear at binding energies beyond 166.0 eV in the S 2p spectrum, suggesting the formation of oxygenated sulfur (SO_x) compound[8], and at 163.5 eV, related to bridging sulfur (P-$[S]_x$-P)[28]. The P 2p spectrum presents new components at 133.1 eV and 134.5 eV, related to the formation of P_2S_x (polysulfides) and PO_x[29], respectively. Additional peaks indicate the presence of other, potentially more complex, compounds. The formation of interphases also contributes to the physical separation of the individual components, due to morphological changes (Fig. 5f-j)[29]. Moreover, we hypothesize that non-linearity of the lattice parameter curve is related to the

7

heterogeneity of the formed SEI, which is also evident from observations made by SEM. This heterogeneity causes a non-uniform current distribution around the NCA particles, which potentially further leads to current hotspots. Due to kinetic limitations in the NCA, these hot spots cause local over-charging that leads to high-stress states and ultimately causing fracturing of the cathode particles and void formation (Fig. 5i, j and Fig. S9)[30]. This fracturing into partially electronic disconnected primary particles and voids results in a lower accessible capacity and subsequently in a higher effective current experienced by NCA particles, which leads, as a consequence, to a further lowering in accessible capacity[29-30]. The lower accessibility is also evident by the overall change in lattice parameters as shown in Fig. 4d (compared to LIC@NCA in Fig. 4h). Nevertheless, in the subsequent cycles, the lattice parameter changes from an approximately exponential decay to a linear behavior (see Fig. S13), suggesting that the formation of SEI is kinetically limiting.

In SSB-LIC@NCA, in contrast, there is no obvious morphological change, neither for LPSCl (Fig. 5c) nor for NCA (Fig. 5n). The physical contact between the individual components remains intact after cycling (Fig. 5o). EDS mapping over the composite cathode cross section reveals an intact In ring around NCA (Fig 5k-m) after 200 cycles, no extra peaks in the In 3d and Cl 2p XPS spectra (Fig. S10) and significant lower intense extra peaks in S 2p spectra, which suggests that the LIC suppresses or modifies the interfacial side reactions while retaining its structural integrity and intimate contact with NCA particles. The XPS of SSB-LIC@NCA (Fig. 4l, m) shows that, in the case of S 2p, the LIC effectively suppresses the formation of oxygenated sulfur (SO_X) compounds beyond 166 eV, while increasing secondary components (162.5-163.7 eV binding energy range). On the other hand, P 2p shows an increase in the secondary components for the SSB-LIC@NCA compared to SSB@NCA. These changes, together with evidence from other techniques, can be interpreted as the formation of a protective layer of reacted LPSCl with the LIC coating. Due to the surface sensitivity of XPS, the results here only provide partial information about the nature of this layer, but it should be related to a better performance and lower degradation of the core NCA. The protective layer has been previously reported as a layer where, upon cycling, Li ions are spontaneously migrating at the cathode │ electrolyte interface, decomposing the positive electrode[31]. Similar reactions may occur as soon as the coating get in contact with LPSCl. Additional reactions between protecting coatings and electrolyte have been recently reported in other cathode architectures that display improved characteristics[28]. Further information on XPS is given

8

in Supplementary Note 2 and Fig. S11, S12. Correspondingly, there is no delay and no non-linear change in regard to lattice parameters (Fig. 4e), during charging and discharging. The improved stability of LIC@NCA compared to NCA is even more prominent after 200 cycles as depicted in the XRD patterns in Fig. 4k. For the composite cathodes containing LIC@NCA, the XRD pattern reveals phases of LPSCl and NCA with minor secondary reflections that can be assigned to Ni_3S_4 and Li_3PO_4 (Fig. S17). Besides, the peak belonging to LIC (Fig. 4j) does not change or show any significant shifting with increasing voltage from ~2 V (OCV) to 4.2V (vs. Li^+/Li), indicating that LIC is stable, and responsible for the improved stability.

3. CONCLUSION

In this study, nano-crystalline halide-based LIC has been tested as a coating for high-voltage cathodes in solid-state batteries to mitigate the degradation of LPSCl and the associated initial discharge capacity loss and poor cycle and rate performance.

First, we synthesized nano-crystalline LIC by high-energy ball milling with an average grain size of nano-scale level and a total conductivity of 1.44 mS/cm after a subsequent annealing step at 300 °C. Thereafter, the LIC was coated around NCA particles by a scalable and economically efficient coating process using mechanofusion. Based on mechanofusion, not only a surface smoothing of NCA particles but also a homogeneous and thin coating of about 150 nm, has been achieved. Finally, solid-state batteries have been assembled with NCA w/wo LIC coating and tested with respect to their cyclability under different C-rates. It is shown that the LIC coating increases the performance at any C-rate at about 80 mAh/g at all C-rates. For example, at 0.1C the discharge capacity reaches a value as high as 148.3 mAh/g compared to 71.8 mAh/g when no coating has been established. Long-cycling tests shows stable long-term cycling with 80.1% capacity retention after 200 cycles under 0.2C compared to SSB-NCA with around 40 mAh/g. The improved performance has been identified to be related to absence of interfacial decomposition reactions of LPSCl, interfacial delamination, and particle cracking, as observed for uncoated NCA-based SSBs.

This study demonstrates that (i) LIC is a promising stable solid electrolyte for coating HV cathodes to enable sulfide-based SSBs when appropriate conditions have been chosen, as well as (ii) that mechanofusion is a viable, easy, and universal technique for coating spherical-shaped cathode materials by complex compounds, which can play a pivot role in

9

the materials development and their scaling, to enable widespread adoption of future solid-state batteries.

4. EXPERIMENT SECTION:

4.1. Synthesis

LPSCl and NCA were purchased from NEI corporation and used as received. Li_3InCl_6 was prepared via a two-step synthesis process: *(i)* Li chloride (LiCl, Sigma-Aldrich, 99.9%) and indium chloride ($InCl_3$, Sigma-Aldrich, 99.99%) were weighed to the stoichiometric molar ratio (3:1) and mechanically mixed in a ZrO_2 container with ZrO_2 balls (diameter = 5 and 10 mm, 1:1, wt.%) in a planetary ball mill (Fritsch, Pulverisette 7) at 500 rpm for 24 h, and *(ii)* The obtained Li_3InCl_6 powder was pelletized at 300 MPa and further annealed at 300 °C with a heating rate of 2 ºC / min for 5 h in Ar atmosphere. The an-LIC was further ball milled for 50 h to prepare fine LIC powder for mechanofusion.

4.2. Coating

1g annealed Li_3InCl_6 (LIC) and 19 g pristine NCA were mixed by mortar and pestle for 30 min to get a homogenous mixture. Thereafter, the powder mixture was into the mechanofusion device (Hosokawa, NOB mode) integrated in a N_2-filled glove box (H_2O and $O_2 < 0.1$ ppm) for 2 h under 3600 rpm.

4.3. Characterization

The morphologies of LPSCl, Li_3InCl_6, and Li_3InCl_6 coated NCA (LIC@NCA) were characterized by a FEI Apreo emission scanning electron microscopy (SEM) equipped with energy dispersive spectroscopy (EDS). X-ray diffraction (XRD) were performed on a Bruker Davinci 1 with a Cu Kα radiation (λ = 1.54178 Å) at room temperature with an air-tight holder to avoid air exposure. The data were collected by scanning 1s per step with a step width of 0.02 from 10° to 70° (2θ). The data for the X-ray refinement were collected by scanning 5s per step with one step of 0.02° from 10 to 70° (2θ). The XRD refinement was done by using the software TOPAS.

Chemical characterization of the samples and the state of the surface was obtained with X-Ray Photoemission Spectroscopy (XPS). Core level spectra were measured using a monochromatized Al Kα (1486.6 eV) line with a hemispherical analyzer at NTNU XPS facilities and a Mg Kα (1253.6 eV) non-monochromatized light and a Specs Phoibos 150 hemispherical analyzer at UAM. Measurements were performed at room temperature and

with chamber pressures below 10^{-9} mbar. The calibration of the binding energy was done using C 1s and Au 4f reference peaks. A Shirley background and asymmetric singlet pseudo-Voigt functions was used to fit the line shape of core levels. The fit was optimized using a Levenberg–Marquardt algorithm[32] and a normalized χ^2 reliability factor.

4.4. Electrochemical measurements

The Li-ion conductivity was measured by adding 0.15 g Li_3InCl_6 or LPSCl (NEI corporation) powder into a PEEK (Polyether ether ketone) cell with a diameter of 10 mm and further pressed at 300 MPa. EIS measurements were carried out at 3-ton pressure and room temperature (25 °C, unless specified), in the frequency range of 10 mHz to 7 MHz with 10 mV of applied sinus amplitude. For half cells, firstly, 80 mg LPSCl was added in the PEEK cell with a diameter of 10 mm and pressed at 3 tons. The cathode composite was prepared by hand-mixing the NCA (LIC@NCA) and LPSCl in a ratio of 7:3 (wt.%) in an agate mortar and pestle inside an Ar-filled glovebox. 9 to 13 mg of as-prepared cathode composite powder was placed on one side of the LPSCl pellet and pressed at 375 MPa.

To prepare the Li-In alloy anode CR2016 coin cells were assembled with In as cathode, Li as anode, and liquid electrolyte (1 M LiTFSI in DOL and DME in 1:1 vol. ratio. After 40 h of Li plating at a current density of 0.25 mA/cm^2 (Fig. S8), the Li-In disk was obtained after cell disassembling, washing with DME, and subsequent drying at 50 °C in an oven inside Ar-filled glovebox. Lastly, the Li-In disc (10 mm diameter) was attached to another side of the LPSCl pellet and pressed at 150 MPa. All the half-cell SSBs were assembled inside an Ar-filled glove box (H_2O < 0.1 ppm, O_2 < 0.1 ppm). The half cells were tested at room temperature (25 °C) and 120 MPa pressure for EIS and GCPL using VMP-300 potentiostat (BioLogic) and Neware battery cycler.

4.5. Operando XRD

For operando XRD measurements, the in-situ cell with a 3 mm diameter was assembled with 1.2 mg cathode composite, 7 mg LPSCl, and Li-In disk. The XRD patterns were collected in a transition mode at beamline SNBL-BM31 at the European Synchrotron Radiation Facility (ESRF) (Swiss-Norwegian Beamline, European Synchrotron Radiation Facility, Grenoble, France) using a monochromatic high brilliant X-ray beam with λ = 0.244860 Å (Data are available in Ref. [33]). The diffractometer is based on a Pilatus2M detector [34] and data processing was done using the BUBBLES software. Before operando measurements, the beam position was optimized to hit more of the cathode side than of the electrolyte.

Data evaluation was performed using the TOPAS V6 software. The PEEK polymer of the cell was modeled with a single peak phase consisting of 12 single reflections, peak positions, and shapes it were extracted from measurements on the empty cell and fixed during multi-dataset processing, allowing only the integrated intensity to vary. Peak shapes of the main phases LPSC and NMC were modeled by the Rietveld method using the Thompson-Cox-Hastings pseudo-Voigt function for the peak shapes.

Notes

The authors declare no competing financial interest.
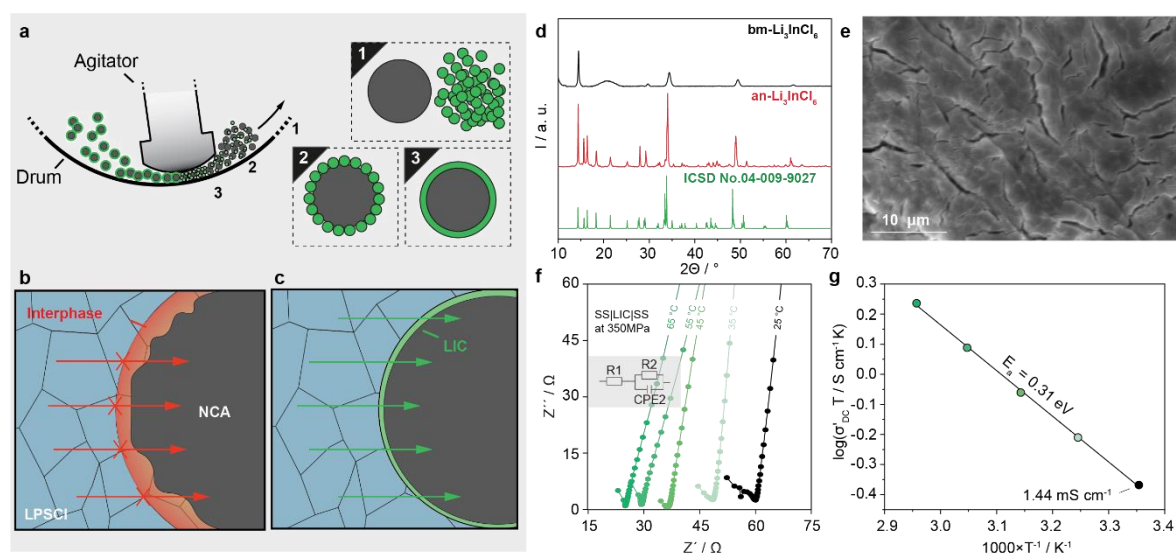
Acknowledgment

Figures

Figure 1. (a) Schematic illustration of mechanofusion and its working principles on coating. (b) Schematic illustration of pristine NCA │LPSCl showing a chemical degradation and formation of resistive CEI at the interface due to parasitic reactions causing hindrance to Li-ion transport. (c) Schematic illustration of LIC@NCA│LPSCl interface representing a stable Li-ion transport without any electrochemical degradation at the interface and the more roundish surface of cathode particles due to the mechanofusion process. (d) XRD patterns of ball milled and annealed LIC powders. (e) SEM images of an-LIC. (f) Nyquist plots of an-LIC under various temperatures with the equivalent circuit used to fit spectra presented in the inset as well as (g) its corresponding Arrhenius plot showing a linear increase in conductivity with temperature with an E_a of 0.31 eV.
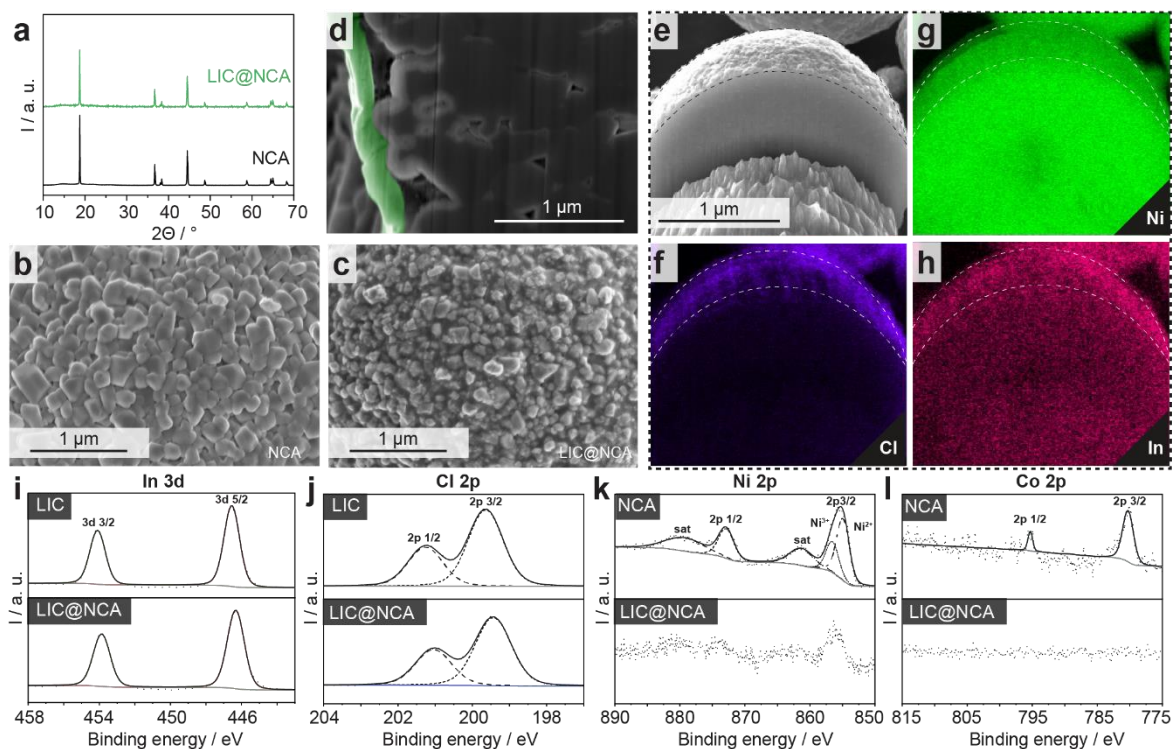
13

Figure 2. (a) XRD pattern collected from the pristine NCA and LIC@NCA particles. SEM images of (b) pristine NCA (b) and LIC@NCA particles (c). (d) Cross-sectional PFIB-SEM image of LIC@NCA showing LIC-coated NCA surface. (e) Cross-sectional FIB-SEM image of LIC@NCA and corresponding EDS mapping (f-h). In 3d (i) and Cl 2p (j) XPS detail spectra for LIC and LIC@NCA and Ni 2p (k) and Co 2p (l) pristine NCA and LIC@NCA.
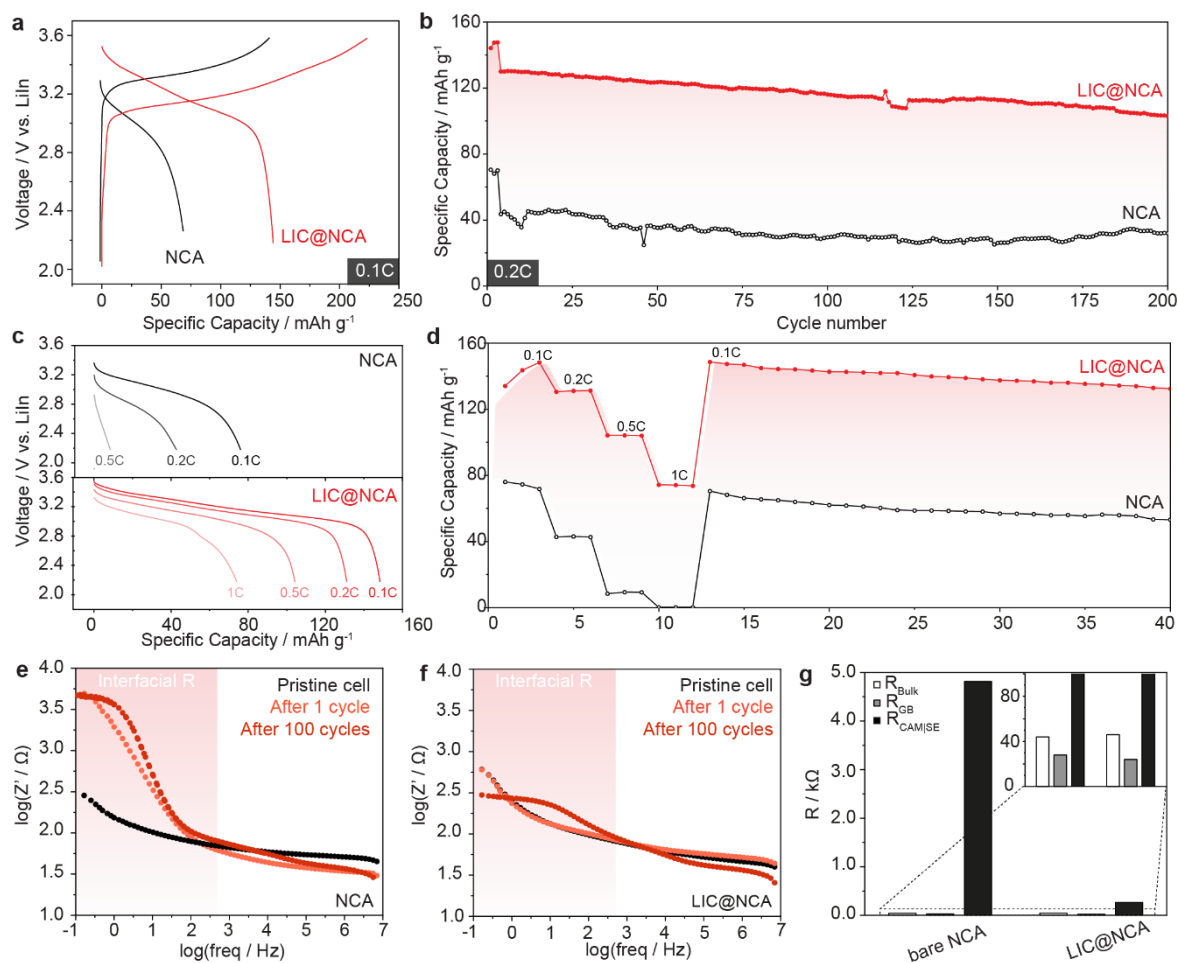
14

Figure 3. (a) Voltage profiles of the pristine NCA and LIC@NCA for the first cycle at 0.1C (b) corresponding long-term cycling behavior at 0.2 C. (c-d) Rate capabilities and corresponding voltage profiles from 0.1 to 1.0 C. Bode plots of the electrochemical impedance of SSB cells based on cathodes with pristine NCA and LIC@NCA (e) before cycling and (f) after cycling (1 cycle and 100 cycles). (g) Summary of the impedance results of cells after 100 cycles. All tests have been performed at 25 °C.
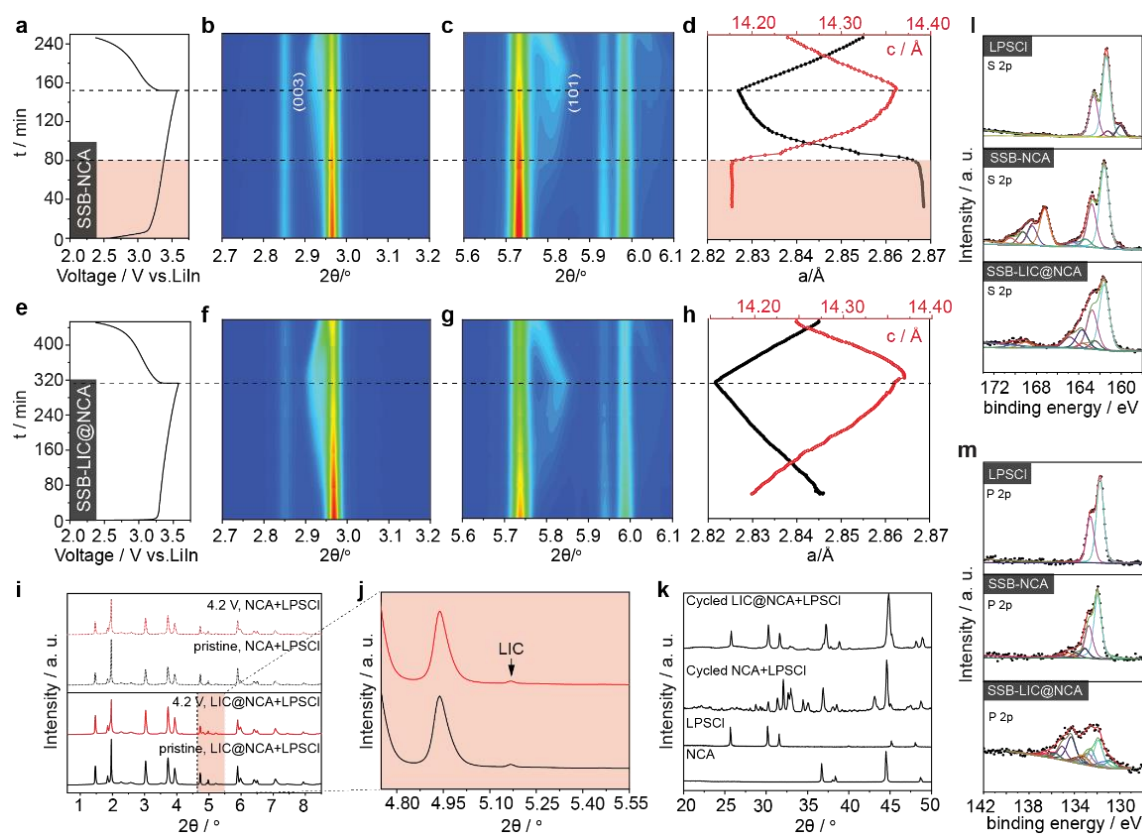
15

Figure 4. Operando XRD data was collected from SSB-NCA (a-c) and SSB-LIC@NCA (e-g) cells in the initial cycle. Contour plots show the evolution of Bragg reflections and the corresponding voltage profile as a function of x(Li). Lattice parameters change for SSB-NCA (d) and SSB-LIC@NCA (h) during the initial cycle. (i-j) SXRD patterns of cathode composites under various voltages. (k) XRD patterns of cycled cathode composites. XPS spectra of (l) S 2p and (m) P 2p of LPSCl, cycled NCA composites, and cycled LIC@NCA composites.
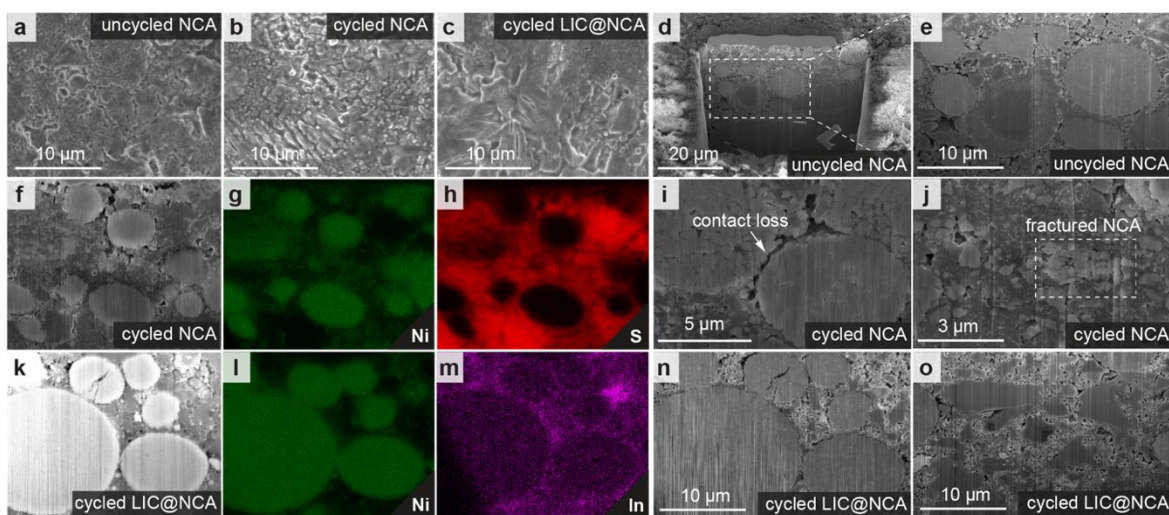
16

Figure 5. Top view (a-c) SEM images of cathodes with pristine NCA and LIC@NCA before and after cycling (200 cycles). PFIB-SEM images of uncycled NCA and LPSCl composite (d-e). PFIB-SEM images of cycled NCA and its corresponding EDS mapping (f-h). Cross-sectional PFIB-SEM images of cycled NCA showing contact loss and NCA particles fracturing (i, j). PFIB-SEM images of cycled LIC@NCA and its corresponding EDS mapping (k-m) confirm the LIC coating on NCA particles. Cross-sectional PFIB-SEM images of cycled LIC@NCA showing intimate particle contacts and no fracturing of NCA particles (n, o).

References

[1]   J. Janek, W. G. Zeier, *Nat. Energy* 2023, **8**, 230.

[2]   J. C. Bachman, S. Muy, A. Grimaud, H. H. Chang, N. Pour, S. F. Lux, O. Paschos, F. Maglia, S. Lupart, P. Lamp, L. Giordano, Y. Shao-Horn, *Chem. Rev.* 2016, **116**, 140-162.

[3]   J. Lau, R. H. DeBlock, D. M. Butts, D. S. Ashby, C. S. Choi, B. S. Dunn, *Adv. Energy Mater.* 2018, **8**, 1800933.

[4]   S. Chen, D. Xie, G. Liu, J. P. Mwizerwa, Q. Zhang, Y. Zhao, X. Xu, X. Yao, *Energy Storage Mater.* 2018, **14**, 58.

[5]   K. J. Kim, M. Balaish, M. Wadaguchi, L. Kong, J. L. M. Rupp, *Adv. Energy Mater.* 2020, **11**, 2002689.

[6]   W. D. Richards, L. J. Miara, Y. Wang, J. C. Kim, G. Ceder, *Chem. Mater.* 2015, **28**, 266.

[7]   Y. Ma, J. H. Teo, F. Walther, Y. Ma, R. Zhang, A. Mazilkin, Y. Tang, D. Goonetilleke, J. Janek, M. Bianchini, T. Brezesinski, *Adv. Funct. Mater.* 2022, **32**, 2111829.

[8]   Y. Ma, R. Zhang, Y. Tang, Y. Ma, J. H. Teo, T. Diemant, D. Goonetilleke, J. Janek, M. Bianchini, A. Kondrakov, T. Brezesinski, *ACS Nano* 2022, **16**, 18682.

[9]   Y. Q. Zhang, Y. Tian, Y. Xiao, L. J. Miara, Y. Aihara, T. Tsujimura, T. Shi, M. C. Scott, G. Ceder, *Adv. Energy Mater.* 2020, **10**, 1903778.

[10]   S. Payandeh, F. Strauss, A. Mazilkin, A. Kondrakov, T. Brezesinski, *Nano Res. Energy* 2022, **1**, e9120016.

[11]   J. Y. Lee, S. Noh, J. Y. Seong, S. Lee, Y. J. Park, *ACS Appl. Mater. Inter.* 2023, **15**, 12998.

[12]   L. Wang, X. Sun, J. Ma, B. Chen, C. Li, J. Li, L. Chang, X. Yu, T. S. Chan, Z. Hu, M. Noked, G. Cui, *Adv. Energy Mater.* 2021, **11**, 2100881.

[13]   X. Li, J. Liang, J. Luo, M. Norouzi Banis, C. Wang, W. Li, S. Deng, C. Yu, F. Zhao, Y. Hu, T.-K. Sham, L. Zhang, S. Zhao, S. Lu, H. Huang, R. Li, K. R. Adair, X. Sun, *Energy Environ. Sci.* 2019, **12**, 2665-2671.

[14]   T. Asano, A. Sakai, S. Ouchi, M. Sakaida, A. Miyazaki, S. Hasegawa, *Adv. Mater.* 2018, **30**, e1803075.

[15]   K. Wang, Z. Gu, Z. Xi, L. Hu, C. Ma, *Nat. Commun.* 2023, **14**, 1396.

[16]   K.-H. Park, K. Kaup, A. Assoud, Q. Zhang, X. Wu, L. F. Nazar, *ACS Energy Lett.* 2020, **5**, 533.

[17]   L. M. Riegger, R. Schlem, J. Sann, W. G. Zeier, J. Janek, *Angew. Chem. Int. Ed.* 2021, **60**, 6718-6723.

[18]   Z. Jiang, S. Chen, C. Wei, Z. Zhang, Z. Wu, Q. Luo, L. Ming, L. Zhang, C. Yu, *Chin. Chem. Lett.* 2023.108561.

[19]   Q. Ye, X. Li, W. Zhang, Y. Xia, X. He, H. Huang, Y. Gan, X. Xia, J. Zhang, *ACS Appl. Mater. Inter.* 2023, **15**, 18878.

[20]   (a) T. Koç, F. Marchini, G. Rousse, R. Dugas, J.-M. Tarascon, *ACS Appl. Energy Mater.* 2021, **4**, 13575-13585; (b) T. Koç, M. Hallot, E. Quemin, B. Hennequart, R. Dugas, A. M. Abakumov, C. Lethien, J.-M. Tarascon, *ACS Energy Lett.* 2022, **7**, 2979-2987; (c) C. Rosenbach, F. Walther, J. Ruhl, M. Hartmann, T. A. Hendriks, S. Ohno, J. Janek, W. G. Zeier, *Adv. Energy Mater.* 2022, **13**,2203673.

[21]   D. H. S. Tan, A. Banerjee, Z. Chen, Y. S. Meng, *Nat. Nano.* 2020, **15**, 170.

[22]   R. Murugan, V. Thangadurai, W. Weppner, *Angew. Chem. In.t Ed.* 2007, **46**, 7778.

[23]   J. K. Feng, B. G. Yan, J. C. Liu, M. O. Lai, L. Li, *Mater. Tech..* 2013, **28**, 276.

[24]   Z. Song, X. Cao, C. Cui, Y. Zhang, J. Liu, F. Li, *Ionics* 2021, **27**, 466.

[25]   M. C. Biesinger, B. P. Payne, A. P. Grosvenor, L. W. M. Lau, A. R. Gerson, R. S. C. Smart, *Appl. Surface Sci.* 2011, **257**, 271.

[26]   A. Banerjee, H. Tang, X. Wang, J. H. Cheng, H. Nguyen, M. Zhang, D. H. S. Tan, T. A. Wynn, E. A. Wu, J. M. Doux, T. Wu, L. Ma, G. E. Sterbinsky, M. S. D'Souza, S. P. Ong, Y. S. Meng, *ACS Appl. Mater. Inter.* 2019, **11**, 4313.

[27]   J. Auvergniot, A. Cassel, D. Foix, V. Viallet, V. Seznec, R. Dedryvère, *Solid State Ionics* 2017, **300**, 78.

[28]   J. S. Kim, S. Jung, H. Kwak, Y. Han, S. Kim, J. Lim, Y. M. Lee, Y. S. Jung, *Energy Storage Mater.* 2023, **55**, 19.

[29]   J. Wang, S. Zhao, A. Zhang, H. Zhuo, G. Zhang, F. Han, Y. Zhang, L. Tang, R. Yang, L. Wang, S. Lu, *ACS Appl. Energy Mater.* 2023, **6**, 3671.

[30]   Y. Han, S. H. Jung, H. Kwak, S. Jun, H. H. Kwak, J. H. Lee, S. T. Hong, Y. S. Jung, *Adv. Energy Mater.* 2021, **11**, 2100126.

[31]   L. R. Mangani, C. Villevieille, *J. Mater. Chem. A* 2020, **8**, 10150.

[32]   M. Schmid, H.-P. Steinrück, J. M. Gottfried, *Surf. and Inter.Analysis* 2014, **46**, 50.

[33]   I. Ellingsen, I., L. Fadillah, F. Jin, Q. H. Nguyen, G. Redhammer, D. Rettenwander, D. European Synchrotron Radiation Facility 2026, https://doi.org/10.15151/ESRF-ES-1185392269.

[34]   V. Dyadkin, P. Pattison, V. Dmitriev and D. Chernyshov, *J. Synchrotron Rad.* 2016, **23**, 825.